A Graphene-Based Flexible Device as a Specific Far-Infrared Emitter for Noninvasive Tumor Therapy

Tingting Yu, Yimin Hu, Guanping Feng, and Ke Hu*

Noninvasive treatments are emerging as a promising strategy not only due to their non-invasive nature, but also due to their additive effects to traditional radiotherapy and chemotherapy. Herein, specific far-infrared rays generated from single-layer, graphene-based devices are applied to tumors as a novel noninvasive therapeutic strategy. In MDA-MB-231 breast cancer cell xenograft and metastasis models, irradiation generated from this flexible device reduces the rate of tumor growth and the number of metastatic nodules per lung by 42% and 55%, respectively. This result might be induced by the similarity between the emission spectra of the device and the absorption spectra of the living tissue. With its high energy conversion and safety, the graphene-based device can serve as an adjuvant therapeutic instrument for combined tumor treatment.

1. Introduction

Surgical resection, radiotherapy, and chemotherapy are the main methods for the treatment of malignant tumors. However, these methods have limitations in clinical practice. For example, the side effects of radio- or chemotherapy may damage neighboring or remote healthy tissues or organs, while surgical tumor resection and postsurgical wound healing may induce distant metastases.[1] The development of noninvasive therapeutic strategies to safely eradicate tumors with fewer off-target effects has become an important research topic.

In contrast to high-energy radiotherapy, treatments based on infrared rays demonstrate low toxicity and good safety.[2] The generation and application of infrared rays are also relatively convenient, as a a transmitting medium is not required, unlike microwave or focused ultrasound therapy.[3] Recently, photothermal therapy based on near-infrared rays has drawn increased interest,[4] with curative efficacy highly sensitive to the targeting capability of nanomaterials.[5] In comparison, treatments based on far-infrared rays do not require additional agents and are mostly used for pain relief and wound healing based on the thermal effects of radiation.[6] The commonly used sources of far-infrared rays are halogen lamps or ceramics; previous work has preliminarily demonstrated that the far-infrared emission could suppress cancer cell proliferation in vitro.[7] However, the electric stability and high temperature of the devices are potential risks in clinical applications and the balance between thermotherapeutic effectiveness and side effects (e.g., low-temperature skin burning or heat shock) remains problematic.[8] Replacement of halogen lamps with carbon fiber-based heating devices does not significantly enhance the curative effects.[9] A safe far-infrared generation source with emission spectra matching those adsorbed by tissues is desirable, as the resonance adsorption would maximize the adsorption efficiency and minimize side effects in living tissue.

Achieving this resonance adsorption requires an understanding of the interaction between far-infrared radiation and the living bodies. Non-absorbed infrared radiation might accumulate on the body surface and induce negative effects such as skin burn. As the characteristic wavelength range of human tissue is approximately 8–14 µm,[6] sources that could generate infrared rays with similar characteristic peaks are essential for clinical application. However, few studies have focused on the development of far-infrared generation devices with high emission density and characteristic peaks at 8–14 µm.

Extensive studies on graphene have shown its unique properties in various research fields,[10] which has generated new possibilities for the exploration of potential applications.[11] Previous studies have shown that the thermal radiation from biased graphene can be used to extract its temperature distribution, carrier densities, and spatial location of the Dirac point. We have previously manufactured low-voltage, flexible graphene heating devices (e.g., 3.7 V), which have been utilized as heating elements in commercial body care products.[12] However, the effect of the emission from such graphene devices on tumors remains unknown.

Dr. T. Yu
Department of Medical Genetics
School of Basic Medical Science & Jiangsu Key Laboratory of Xenotransplantation
Nanjing Medical University
Nanjing 211166, China

Dr. Y. Hu, Prof. G. Feng
Grahope New Materials Technologies Inc.
Shenzhen 518063, China

Dr. K. Hu
Key Laboratory of Clinical and Medical Engineering
Department of Biomedical Engineering, School of Biomedical Engineering and Informatics
Nanjing Medical University
Nanjing 211166, China
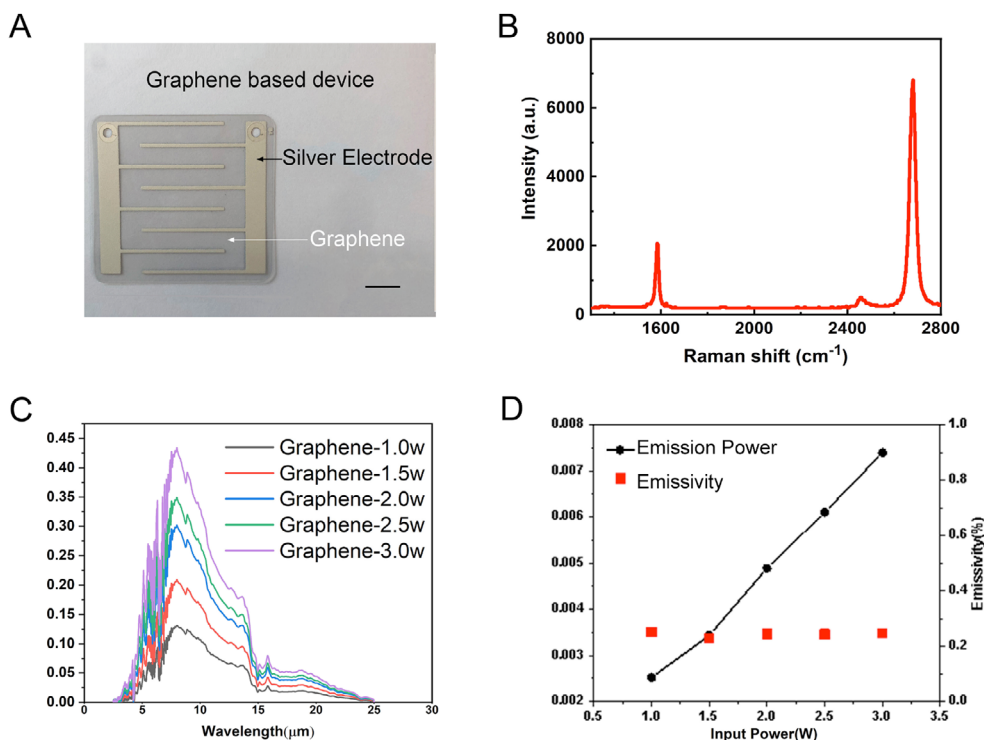E-mail: kehu@njmu.edu.cn

Figure 1. Graphene-based flexible electronic devices demonstrate good specific far-infrared ray generation. A) Photograph of a graphene-based device. B) Raman spectrum of the graphene used for the device. C) Far-infrared emission spectra of a graphene-based device under different input powers (1, 1.5, 2, 2.5, and 3 W). D) The emission power and emissivity of a graphene-based device under different input powers (1, 1.5, 2, 2.5, and 3 W).

The results of the present study are the first to demonstrate the potential use of far-infrared rays generated by a graphene-based heating device for tumor treatment. The emission spectrum of the graphene made by chemical vapor deposition (CVD) coincides with the absorption spectra of nude mice and the human body. We demonstrated the effectiveness of the device by comparing the effects of treatment of far-infrared rays generated by graphene and carbon fiber-based devices on tumors subcutaneously transplanted to nude mice. The far-infrared rays generated by graphene showed superior infrared transduction, which was further validated by the stronger induction of apoptosis in classic monolayer and 3D multicellular spheroid culturing models.

2. Results and Discussion

2.1. Specific Far-Infrared Ray Generated by a Single-Layer Graphene Electronic Device

The single-layer graphene used in the device was prepared by CVD and transferred from the copper foil to a polyethylene terephthalate (PET) membrane (**Figure 1**A). Raman spectroscopy verified the single-layer nature of the graphene film (Figure 1B).[13] The excellent electrical stability and flexibility of the device were demonstrated in bending tests in which the resistance of the device remained constant when the device was bent 100 times at different curvatures (Figure S1D, Support-

ing Information). The far-infrared rays emitted by this device were first measured using a far-infrared radiation detector card (Figure S1C, Supporting Information). The emission spectrum shown in Figure 1C indicated a characteristic emission peak of the graphene device at approximately 8.0 µm. This characteristic emission peak changed slightly with input power, contrary to Planck's radiation law but consistent with a recent report by Luo et al.[14] We believe this phenomenon was caused by both the characteristics radiation of graphene and the resonance between the graphene and PET membrane inside the device. The emission power was further measured by radiometer at test wavelengths ranging from 0.19 to 20 µm (Figure 1D). Based on the far-infrared emission spectra, the power emissivity of the sample was about 2.5%. The emissivity was calculated as follows.

$$M = \frac{2\pi h c^2}{\lambda^5} \cdot \frac{1}{e^{hc/(\lambda KT)} - 1} \tag{1}$$

$$M = \pi L_\lambda \tag{2}$$

$$L_\lambda = c\omega_\lambda \tag{3}$$

From the Planck's and Lambert's radiation laws, ω_λ is the spectral energy density of radiation, L_λ is the spectral radiance, and M is the spectral radiant exitance. Thus, the power emissivity of the sample is on the order of a few thousands.

We further evaluated the efficiency of this single-layer graphene device as a far-infrared radiation emitter using a commercially available device based on carbon fibers as a
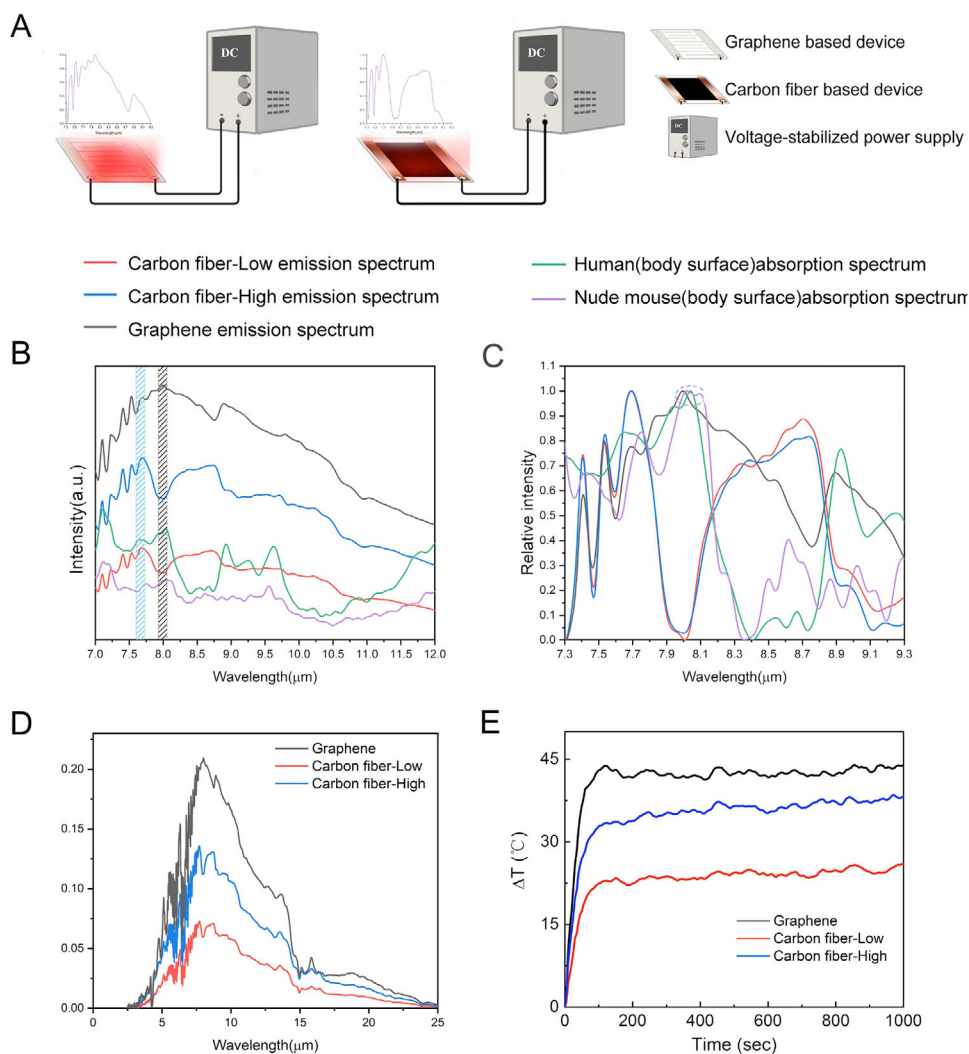
ADVANCED
SCIENCE NEWS
www.advancedsciencenews.com

ADVANCED
THERAPEUTICS
www.advtherap.com

Figure 2. Specific far-infrared rays generated by graphene-based flexible electronic devices are more effectively absorbed than those generated by carbon fiber-based devices due to the higher resonance effect on tissues in vivo. A) Diagram of the generation of far-infrared rays by graphene-based and carbon fiber-based devices. B) Far-infrared emission spectra of graphene-based devices (1.5 W), carbon fiber-based devices (1.5 and 2.5 W), nude mice (body surface), and humans (body surface). C) Normalized spectra. D) Far-infrared emission spectra of graphene-based and carbon fiber-based devices under certain input powers (graphene: 1.5 W, carbon fiber-low: 1.5 W and carbon fiber-high: 2.5 W). E) Thermogenesis curves of the graphene-based and carbon fiber-based devices with different input powers. Dark and jade patterns and blue circles mark the major characteristic peaks of each spectrum.

reference (Figure S1A, Supporting Information). The far-infrared rays generated by the graphene-based or carbon fiber-based devices were obtained using a Fourier transform infrared spectrometer (**Figure** 2A). The absorption spectra of nude mice and the human body were also measured. The characteristic absorption peaks of the nude mice and human body surface were approximately 8.0 μm, which matched the emission peak position of the graphene device (≈8.0 μm). In contrast, the emission peak wavelength of the carbon-fiber devices was below 7.7 μm for both low and high power inputs (Figure 2B). The normalized data shown in Figure 2C further illustrate the overlap between the emission peak of the graphene device and the absorption peak at ≈8.0 μm. Additional measurements showed that the characteristic emission peaks were rarely sensitive to power inputs between 1 and 3 W for both the graphene- and carbon-fiber devices

(Figures S2 and S3, Supporting Information). The differences in the emissive spectra of far-infrared rays generated by these two types of carbon-based device might be attributed to the micro-nanostructures of graphene and carbon fiber (Figure S1B, Supporting Information). The surface temperature measurements (Figure 2E; Figure S1E, Supporting Information) demonstrate higher far-infrared ray generation efficiency of the graphene devices than that for the carbon fiber-based devices of the same size. We also included a commercially available halogen lamp-based device as an additional control (Figure S4A, Supporting Information). The infrared emission peak of the halogen lamp was approximately 7.5 μm (Figure S4B, Supporting Information). The differences between the infrared emission peaks of the halogen lamp and the absorption peaks of the nude mice and the human body were even larger (Figure S4C,D, Supporting Information).

**ADVANCED
SCIENCE NEWS**

www.advancedsciencenews.com

**ADVANCED
THERAPEUTICS**

www.advtherap.com

2.2. Far-Infrared Ray Generated by Graphene-Based Devices Induced Tumor Cell Apoptosis

Given that the graphene-based device was able to generate radiation more efficiently than the carbon fiber-based device, MDA-MB-231 breast cancer cells and PC3 prostate cancer cells were next subjected to apoptosis assays to evaluate the ability of these two devices to induce apoptosis. The results demonstrated that the far-infrared radiation generated by the graphene-based device induced higher apoptosis ratios in both cell lines compared to the ratios in the carbon fiber-based device under the same input power (**Figure 3**A—G; Figure S5, Supporting Information). Similarly, treatment with a graphene-based device more significantly affected tumor cell viability (Figure S6, Supporting Information) and inhibited MDA-MB-231 and LoVo colon cancer cells from forming anchorage-dependent foci in culture (Figure 3; Figure S7A–B, Supporting Information). Compared to cells treated with the carbon fiber-based device, the MDA-MB-231 and LoVo cells irradiated by the graphene-based device showed weakened invasion and migration (Figure 3J–L; Figure S7C–D, Supporting Information).

2.3. Strong Penetrating Ability of Far-Infrared Rays Generated by Graphene-Based Devices

To further compare the tumor suppression properties of the far-infrared radiation emitted by the graphene-based and carbon fiber-based devices in vitro, a 3D multicellular spheroid model was established by culturing LoVo cells on an anisotropic magnetic hydrogel platform based on our previous work (**Figure 4**A).[15] After 15 min of treatment at the same power, the live and dead cells were fluorescently labeled green and red, respectively. Tumor multicellular spheroids are less sensitive to heat than cells in monolayer culture.[16] As shown in Figure 4B,C, almost all cells were dead after exposure to the far-infrared radiation generated by the graphene-based device. However, there were relatively more living cells inside the multicellular spheroid treated with the carbon fiber-based device (Figure 4D). Flow cytometry analysis indicated that treatment therapy with the graphene-based device led to apoptosis of 58.17% of the LoVo cells, compared to 21.64% with the carbon fiber-based device (Figure 4E–H), indicating the stronger penetrating ability of the far-infrared radiation generated by the graphene-based device. Moreover, halogen lamp treatment did not induce significant LoVo cell apoptosis or death in either 2D or 3D cultures (Figures S8–S10 and Table S1, Supporting Information).

2.4. Far-Infrared Rays Generated by Graphene-Based Devices Suppressed Xenograft Tumor Growth

To explore the tumor-suppressing effect of the far-infrared radiation emitted by graphene in vivo and to determine the appropriate treatment power, PC3 prostate xenograft tumor-bearing mice were subjected to far-infrared treatment with a graphene-based device. At present, the temperature of clinical moderate hyperthermia is generally 39.5–45 °C. Thus, we set the highest treatment power of the graphene-based device to 1.5 W, which resulted in a surface temperature of nude mice at around 42 °C after 30 min of irradiation. Figure S11, Supporting Information, shows the infrared thermography of mice before and immediately after treatment. These images may also reflect the temperature distribution inside the tumor since the xenograft tumors were located beneath the skin and temperature changes could be clearly observed. Figure S11A,B and Figure S11C,D, Supporting Information, show the temperatures of the tumors before and after irradiation with graphene and carbon fiber devices, respectively. The temperatures of the tumors were higher than 42 °C after irradiation with both types of devices, which matched the temperatures currently defined for clinical hyperthermia and will not cause low-temperature burns. No acute side effects were observed on any mice after any single irradiation. As the intensity of the far-infrared radiation increased from 1 to 1.5 W, the weight and volume of the tumors decreased significantly (Figure S12A–B, Supporting Information). In addition to inhibiting tumor growth, the far-infrared rays generated by the graphene-based devices had a therapeutic effect on tumors as evidenced by the prolonged survival of the tumor-bearing mice (Figure S12D, Supporting Information). Histological sections of PC3 xenograft tumor samples showed decreased Ki-67 staining with increasing far-infrared radiation intensity generated by the graphene-based device (Figure S12E, Supporting Information). During treatment, the mice did not show a significant loss in body weight (Figure S12C, Supporting Information). To provide an intuitive comparison of tumor suppression between the far-infrared radiation emitted by the graphene-based and carbon fiber-based devices, an MDA-MB-231 xenograft tumor model was established by subcutaneously injecting 4×10^6 tumor cells into the backs of female BALB/c nude mice. When the tumors grew to 50–100 mm³, the tumor-bearing areas were irradiated with the graphene-based or carbon fiber-based devices twice daily for 20 min each time (**Figure 5**A). The input power for the graphene-based device was 1.5 W, while the input powers for the carbon fiber-based device were 1.5 W (CF-Low) and 2.5 W (CF-High, which resulted in a stabilized surface temperature of nude mice at 42 °C after 30 min of irradiation). The tumors were measured weekly for 5 consecutive weeks and each tumor was individually weighed after the mice were euthanized. Under the same input power, the tumor growth rate of the graphene-treated group was reduced by 42%, which was much slower than that in the carbon fiber-treated group (Figure 5B–D). Furthermore, even when the input power of the carbon fiber-based device was increased by 1 W, the tumor suppression effect was less than that of the graphene-based device (Figure 5B–D). The final weights of the tumors were consistent with the experimentally observed tumor growth and the tumors in the graphene-treated group weighed less (Figure 5E). Although the high-power carbon-fiber device also had an inhibitory effect on tumor growth, it caused weight loss due to the thermal side effect of the far-infrared rays, which the nude mice could not absorb (Figure 5F). The histological sections showed that xenograft tumors from the graphene-treated group had the least Ki-67 staining, suggesting benign growth relative to that of the carbon fiber-treated group exposed to the same or even higher power (Figure 5G). Image analysis showed that the graphene-treated group had the lowest number of Ki-67-positive cells (Figure 5H).
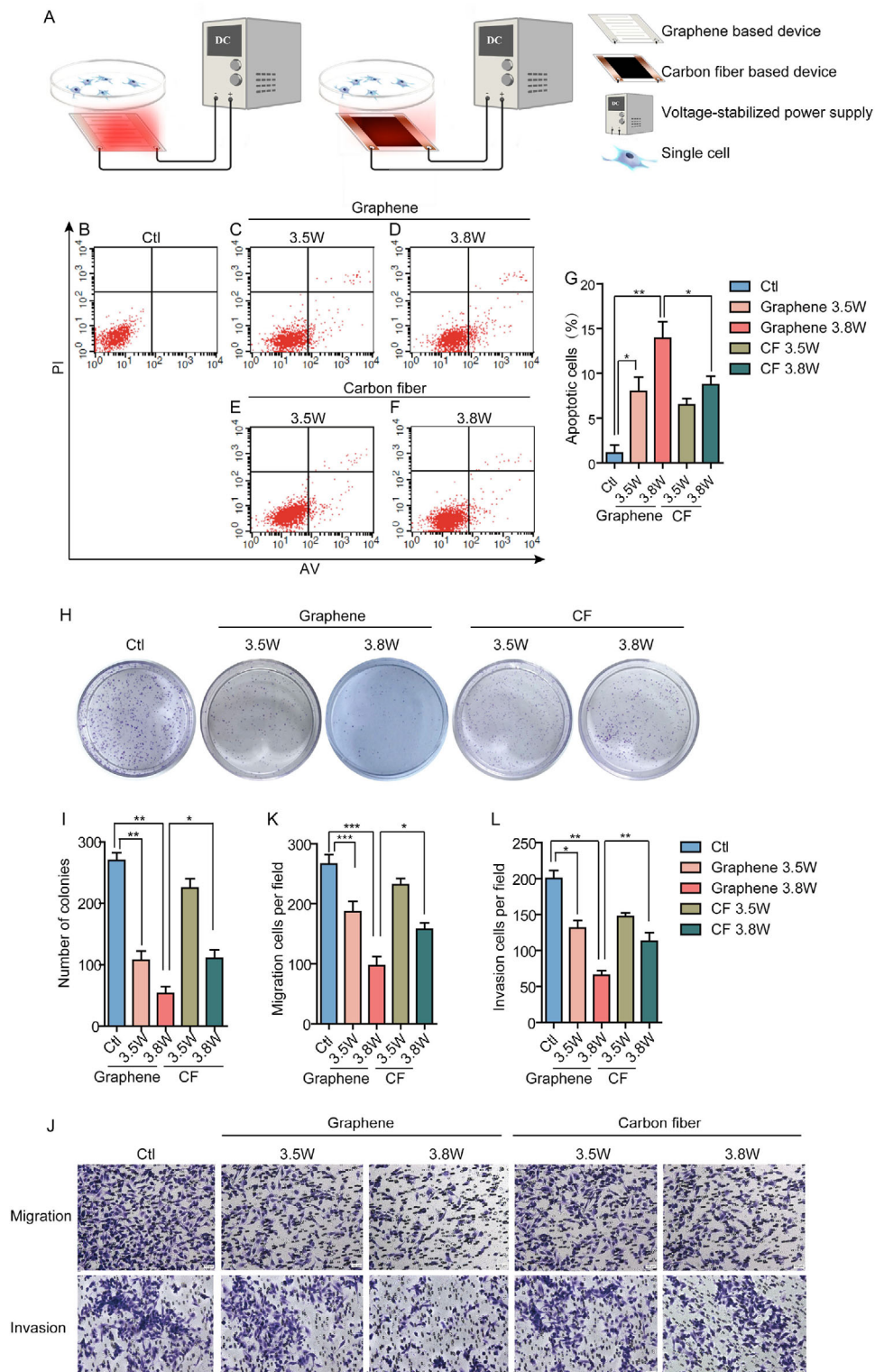
1900195 (4 of 11)

Figure 3. Far-infrared radiation treatment with graphene-based devices suppresses the malignant phenotype of MDA-MB-231 tumor cells. A) Diagram of the far-infrared treatment of MDA-MB-231 tumor cells with graphene-based and carbon fiber-based devices. B–F) Apoptosis assays of the far-infrared treatment with both devices. Apoptosis and necrotic cell death were assessed by double staining with annexin V/FITC and propidium iodide (PI). G) Percentages of apoptotic cells in (B–F). H) Crystal violet staining of the clones formed by MDA-MB-231 tumor cells 14 days after far-infrared treatment. I) Quantification of the clones in (H). J) Migration and invasion assays of MDA-MB-231 tumor cells treated with far-infrared radiation. K–L) Quantification of the migration and invasion of the cells in (J).
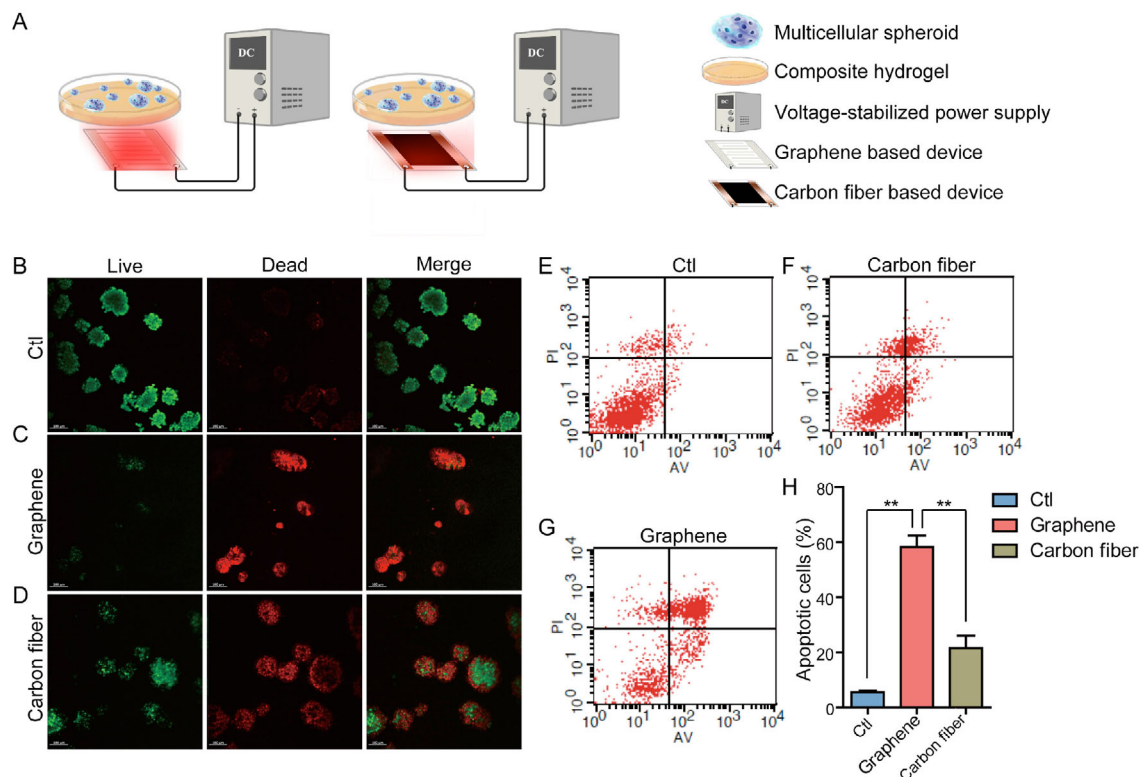
Figure 4. Far-infrared radiation generated by graphene-based devices penetrates multicellular spheroids to induce LoVo tumor cell apoptosis. A) Diagram of the far-infrared treatment of LoVo multicellular spheroids with graphene-based and carbon fiber-based devices. B–D) Live/dead assays of multicellular spheres of LoVo colon cancer cells receiving far-infrared treatments from graphene-based or carbon fiber-based devices. E–G) Flow cytometry analysis of apoptotic cells treated with far-infrared radiation emitted by graphene-based and carbon fiber-based devices. H) Percentages of apoptotic cells in (E–G). Scale bar: 100 µm.

2.5. Far-Infrared Rays Generated by Graphene-Based Devices Suppressed Tumor Metastasis

MDA-MB-231 cells are triple-negative (estrogen receptor⁻ progesterone receptor⁻human epidermal growth factor receptor2⁻ [ER⁻PR⁻Her2⁻]) breast cancer cells with high metastatic potential. To evaluate the efficacy of far-infrared treatment for metastatic tumors, 1×10^6 luciferase-labeled MDA-MB-231-Luc cells were injected into the tail vein of each athymic mouse (**Figure 6**A). Luciferase photon fluxes were monitored each week and representative noninvasive bioluminescence images at week 6 postinjection are shown in Figure 6B. As expected, the tumors that received far-infrared radiation emitted by graphene devices had lower fluorescence intensity than those in the other two carbon fiber-treated groups (Figure 6C). The numbers and volumes of metastatic nodules in the lungs taken from graphene-device-treated mice were consistently and significantly reduced by 55%, which was much less than those reductions in the mice in the carbon fiber groups treated at the same or even higher power (Figure 6D–F). Moreover, the mice in the CF-High group were depressed during treatment, with three mice stopping breathing during anesthetic preparation before injection of the luciferase substrates, suggesting strong side effects of the high-power carbon fiber-based treatment.

The absorption efficiency of far-infrared rays depends on the match degree between the emission property of far-infrared ray and absorption property of the irradiated subjects. The absorption rate increases with the degree of matching.[17] Based on the resonance adsorption theory, the nude mice and human body should absorb radiation more efficiently from the graphene-based device than from the carbon-fiber device. Figure 1C further shows the similarity between the emission spectrum of the graphene device and the adsorption spectra of nude mice and the human body after normalization of the spectra with the min–max standardization method. The characteristic absorption peak of the nude mice and human body surfaces matched the characteristic emission peak of the graphene device at a wavelength of 8.0 µm. In contrast, the highest emission peak of the carbon-fiber devices was 0.3 µm away from the adsorption maximum of the nude mice and human body surface. The similarity degree and average Euclidean distance between the absorption spectra of nude mice/human body and the emission spectra of the graphene/carbon-fiber devices have also been compared.[18] In the wavelength window of 8.0 ± 0.5 µm, the similarity degree between the absorption spectrum of nude mice and the emission spectrum of the graphene device was an estimated 0.49 ± 0.05 and 0.35 ± 0.06 for the human body surface. In comparison, the similarity degrees between the nude mice/human body and carbon-fiber and halogen lamp devices were all negative in the same wavelength range. Correspondingly, the average Euclidean distance between the spectrum of the nude mice/human body surface and that of the graphene device was larger than that
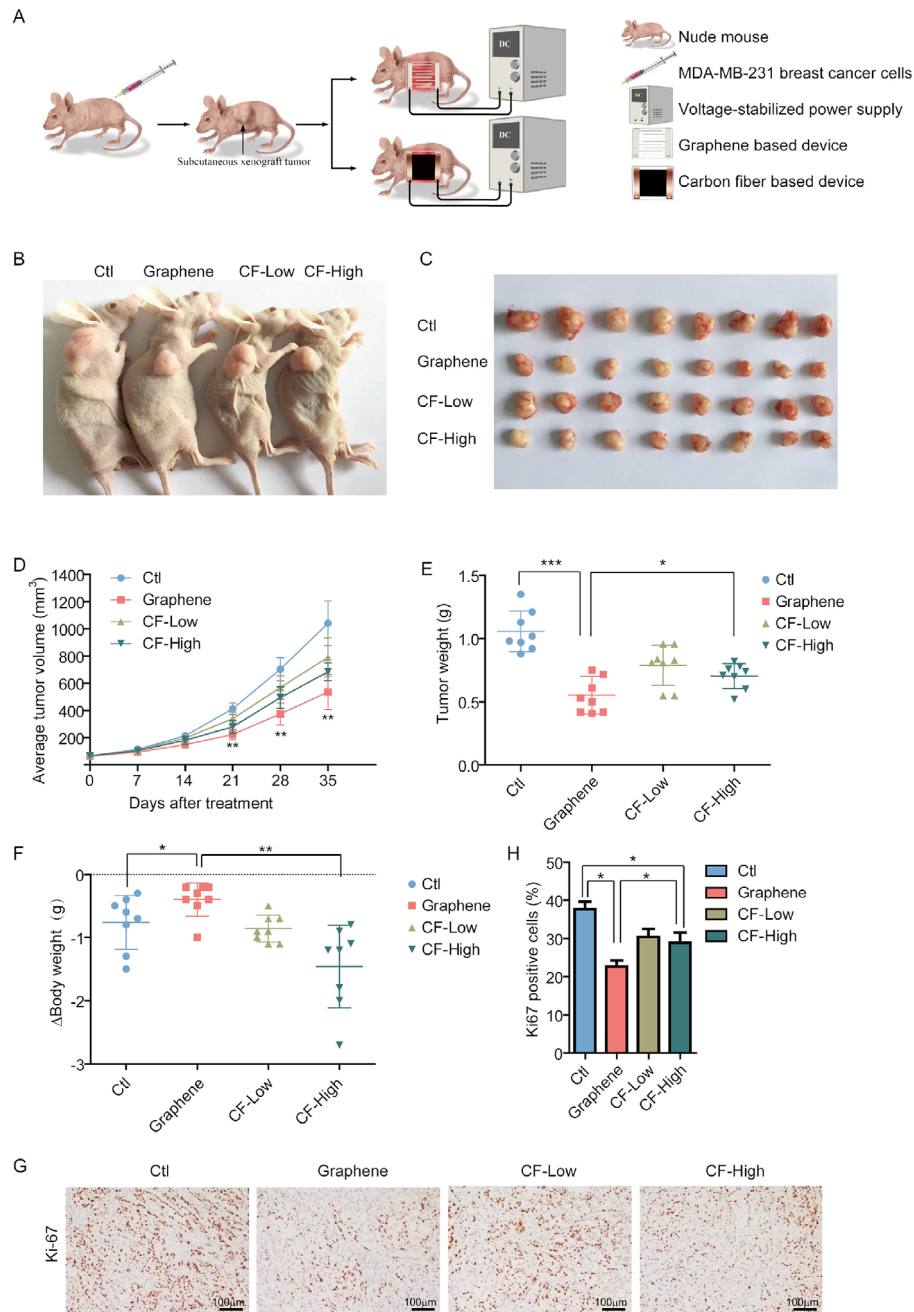
**ADVANCED
SCIENCE NEWS**

www.advancedsciencenews.com

**ADVANCED
THERAPEUTICS**

www.advtherap.com

Figure 5. Far-infrared radiation treatment with graphene-based devices suppresses xenograft tumorigenesis of MDA-MB-231 tumor cells. A) Diagram of far-infrared treatment for MDA-MB-231 tumor-bearing mice with graphene-based and carbon fiber-based devices. B) Representative images of tumor-bearing nude mice in each group at the end of the 5-week observation period. C) MDA-MB-231 xenograft tumors taken from tumor-bearing nude mice at the end of a 5-week observation period. D) Weekly measurements of average tumor volumes. E) Ranges of individual terminal tumor weights. F) Ranges of individual weight loss at the end of the far-infrared radiation treatment. G) Immunohistochemistry (IHC) staining of the xenograft tumor sections for the proliferative antigen Ki67. The original objective magnification is 10×. H) Quantification of Ki67-positive tumor cells in the xenograft tumor sample sections. Five images were randomly selected from each experimental group for Ki67-positive cell counts.

between the spectrum of the nude mice/human body surface and that of carbon-fiber devices (Table S2, Supporting Information). These results supported the assumption that the nude mice/human body surface more efficiently adsorbs far-infrared rays generated by the graphene device than those generated by the carbon-fiber and halogen lamp devices.

Poor penetration has traditionally limited the clinical application of far-infrared radiation. The xenograft and metastasis tumor models in the present study showed that the far-infrared radiation produced by graphene more strongly inhibited tumor growth and metastasis. Hyperthermia treatments are reported to slow the growth rate of xenografted tumors by 20%; in contrast,
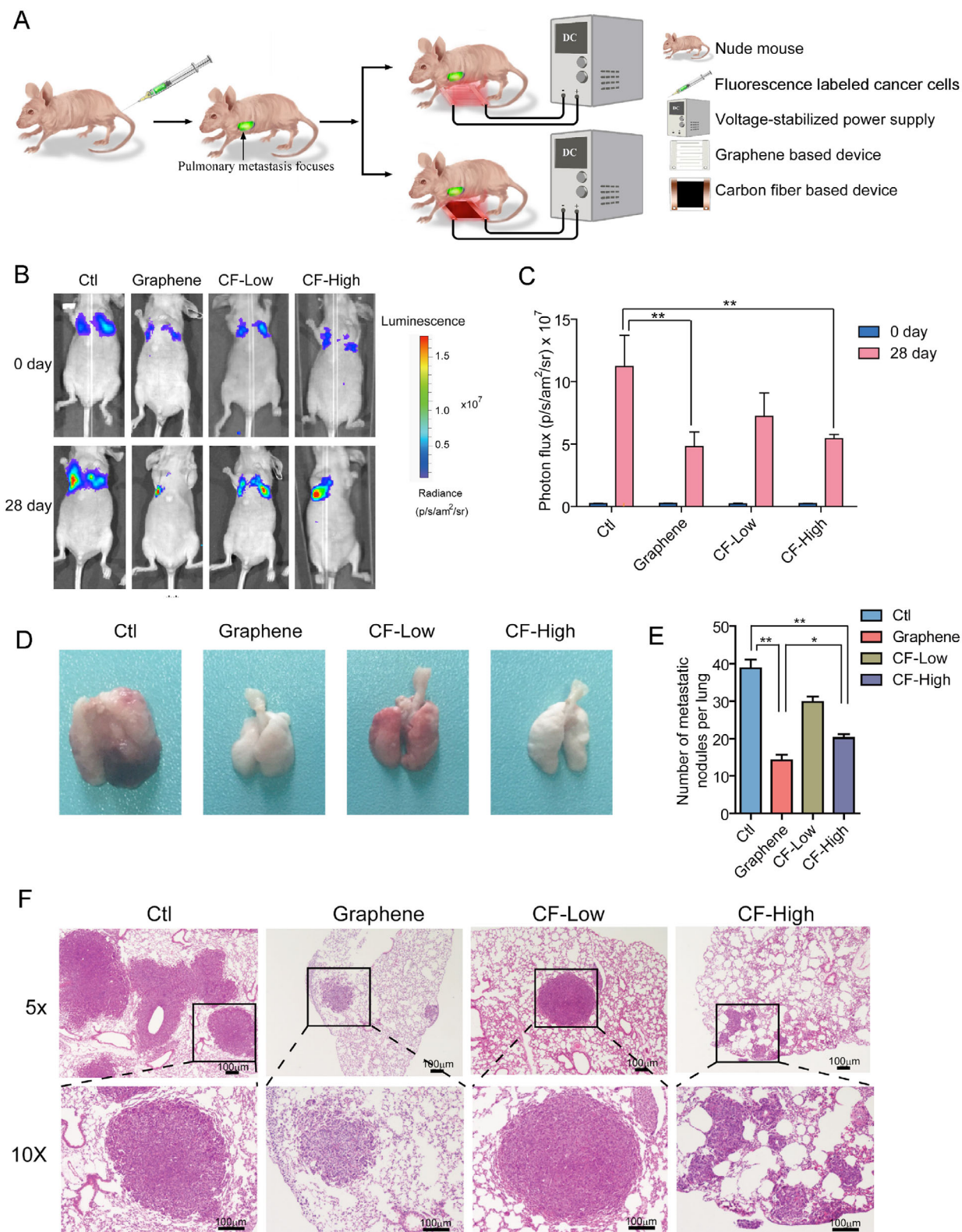
Figure 6. Far-infrared radiation treatment based on graphene-based devices inhibits breast cancer metastasis in vivo. A) Schematic of experimental metastasis by tail vein injection of luciferase-labeled MDA-MB-231-Luc cells and subsequent far-infrared therapy with graphene-based and carbon fiber-based devices. B) Representative bioluminescence images showing lung metastasis in each experimental group. C) Measurements of photon fluxes after 28 days of treatment with graphene-based and carbon fiber-based devices. D) Representative images of lungs 28 days after far-infrared treatment. E) Numbers of metastatic nodules in the lungs according to experimental group. F) Hematoxylin and eosin (HE) staining showing lung metastases.

our data demonstrated a 42% tumor growth rate inhibition in the graphene-based device treated group.[19] Our results are comparable to those for contemporary photothermal therapy, which alone (without other types of therapies such as immunotherapy) inhibits the growth rates of aggressive tumors by ≈40–50%.[20] However, unlike the devices described in the present study, photothermal therapy requires the preadministration of nanoparticles to patients, which raises concern for clinical safety. Since it was difficult to detect the specific penetration depth of the far-infrared radiation in vivo, we constructed an in vitro 3D tumor multicellular spheroid model for verification. This multilayered, compact 3D structure with high thermoresistence mimics tumor growth in vivo. In the 3D model, the apoptotic ratio of the graphene/carbon fiber treated group was 2.69 (58.17% vs 21.64%) and 1.40 (13.15% vs 9.42%) in the classic monolayer model (Figures 3G and 4H). Moreover, the halogen lamp had almost no effect on inducing apoptosis in the 3D model (Figure S10, Supporting Information). These results indicated that in the multilayer structure, the far-infrared radiation generated by the graphene had a stronger penetrating ability than that generated by the carbon fiber and halogen lamp devices. We also observed increased graphene-induced apoptosis in 2D cultured tumor cells than those in the carbon fiber and halogen lamp devices (Figure 3B–G; Figures S8 and S9, Supporting Information), implying unique characteristics of the far-infrared radiation generated by graphene.

Comprehensive cancer treatment is the current development trend. Far-infrared radiation is a physical therapy method with analgesic, anti-inflammatory, and chemotherapeutic sensitization effects. Based on the superiority of far-infrared generated by graphene in inhibiting tumor growth, it may also have a stronger adjuvant therapeutic effect with chemotherapy and be effective in alleviating side effects. Future work will focus on precisely measuring the tumor temperature to better understand the relationship between increased temperature and tumor growth inhibition—in other words, to determine the dependency of tumor inhibition on tumor heating. This will eventually lead to the identification of factors other than heat that contribute to tumor inhibition—for instance, infrared radiation. After fully elucidating the mechanism, we can design combinational therapeutic plans such as the combination of radiotherapy, chemotherapy, and infrared radiation generated by graphene-based devices and test the tumor therapy effects on large animals with complete immune systems, and ultimately achieve increased inhibition of tumor growth and metastasis.

3. Conclusion

To our knowledge, this study is the first to report that specific far-infrared radiation emitted by a graphene-based device effectively suppressed tumor growth and prolonged survival in tumor-bearing mice. The resonance effect improved the tissue absorption of far-infrared rays generated by the graphene devices. Given the antiphlogistic and analgesic effects of far-infrared rays, we believe that this safe device, which provides a high-energy transformation rate, could serve as an adjuvant therapeutic instrument for combined tumor treatment.

4. Experimental Section

Cell Culture: MDA-MB-231 cells were maintained in L-15 medium containing 1% penicillin and streptomycin supplemented with 10% fetal bovine serum. The PC3 and LoVo cells were maintained in Dulbecco's Modified Eagle Medium containing 1% penicillin and streptomycin supplemented with 10% fetal bovine serum. All cells were cultured at 37 °C with 5% CO_2.

Apoptosis Assay: After 15 min of far-infrared radiation, apoptotic cells were analyzed using an annexin V-PI apoptosis detection kit by flow cytometry.

Colony Formation Assay: After 15 min of far-infrared radiation, 1×10^3 MDA-MB-231 or LoVo tumor cells were cultured in 60 mm Petri dishes for 14 days. The plates were then fixed with 4% paraformaldehyde and stained with crystal violet; colonies containing more than 50 cells were counted.

Migration and Invasion Assay: The in vitro cell motility and invasion assays used 24-well plates (Millipore) with transwell chambers with a polyester (PET) filter membrane containing 8.0 μm pores. For the coating of the invasion assay, Matrigel was diluted to 0.3 mg mL^{-1} with a coating buffer (0.01 M Tris, 0.7% NaCl, pH 8.0), and 60 μL Matrigel were coated onto the upper compartment of the cell culture insert. After incubation for 1 h at 37 °C, the cell culture insert was ready for seeding. After 15 min of far-infrared radiation, MDA-MB-231 or LoVo tumor cells (5×10^4 and 1×10^5 cells per well for the migration and invasion assays, respectively) were seeded into the cell culture insert with serum-free media with 10% fetal bovine serum used as a chemoattractant. After 8 h (migration) or 12 h (invasion) of incubation at 37 °C, the migrated or invaded cells were stained with 0.1% crystal violet (Beyotime). The cell images were photographed with an Axiovert 200 inverted microscope (Zeiss, Germany) at 200× magnification and cells in three random fields of view were counted.

Multicellular Spheroid Culture: A multicellular spheroid culture were used as the cell culture model as previously described.[15] Briefly, the anisotropic magnetic hydrogel was first rinsed twice with phosphate-buffered saline (PBS) and then sterilized with ethylene oxide before cell seeding. Then, the magnetic hydrogel was sliced and incubated with cell culture medium for 12 h before cell culture. A single suspension of LoVo cells (1×10^6 cells mL^{-1}, 50 μL) was grown on sliced magnetic hydrogels placed in 6-well cell culture plates. Following the initial cell plating, the tumor cells were allowed to adhere to the hydrogel before the addition of complete growth medium to 3 mL. All cultures were maintained in an incubator at 37 °C in 5% CO_2. The live/dead cells were stained with the LIVE/DEAD Cell Imaging Kit (488/570) (Thermo Fisher, R37601).

Xenograft Tumor Model: MDA-MB-231 cells were suspended in PBS and mixed in a 1:1 ratio with Matrigel. A 100-μL suspension containing 4×10^6 MDA-MB231 cells was subcutaneously injected into the left subaxilla of BALB/c nude mice. The mice were monitored weekly and the tumor volume was calculated using the equation volume = (length × width^2)/2. For the PC3 xenograft tumor model, a 100-μL suspension containing 1×10^7 PC3 cells was subcutaneously injected into each nude mouse.

Metastasis Tumor Model: A total of 1×10^6 luciferase-labeled MDA-MB-231 cells were injected into the tail vein of each athymic nude mouse. The mice were monitored weekly by in vivo bioluminescence imaging. For stable luciferase expression, the mice were imaged within 5 min of a post-intraperitoneal injection of 100 mg kg^{-1} luciferin (200 μL of a 10 mg mL^{-1} stock solution).

Far-Infrared Radiation Treatment: For the monolayer cell culture model, the input power of the graphene-based and carbon fiber-based devices was set as indicated in Figure 2 and Figure S3, Supporting Information, with a radiation time of 15 min. For the multicellular spheroid model, the input powers of the graphene-based and carbon fiber-based devices were set at 3.5 W. For the xenograft and metastasis tumor models, the input power of the graphene-based device was set at 1.5 W, while those of the carbon fiber-based device were set at 1.5 and 2.5 W. The animals were radiated for 20 min, twice daily. The Committee on the Ethics of Animal Experiments of Nanjing Medical University approved all animal experiment protocols.

Infrared Emission/Absorption Spectrum Characterization and Analysis: All measurements were carried out at room temperature (25 °C). The

infrared emission spectra were collected using a Fourier transform infrared spectrometer (Thermo Fisher, Nicolet iS50). The light source was set as external, deuterated triglycine sulfate (DTGS) was selected for the detector, and KBr was used for the beam splitter. A single beam was selected as the final format, with a range of 400–4000 cm^{-1}, a resolution of 8 cm^{-1}, and a total of 48 scans. The abscissa was converted to wavelength to obtain the final spectrum. The infrared absorption spectrum was also measured using the Fourier transform infrared spectrometer (Thermo Fisher, Nicolet iS50). An attenuated total reflectance (ATR) external fiber optic probe assembly with Ge probe material was connected to the Fourier infrared spectrometer equipment through a coupler. The light source was IR, DTGS was selected for the detector, and KBr was used for the beam splitter. The determination range was 400–4000 cm^{-1}, the resolution was 8 cm^{-1}, and a total of 64 scans were collected. First, the probe was placed in the air to collect background data. The probe was then kept close to the surface of the subject (mouse or human body) and then pressed for approximately 1 min to collect data. The obtained data were processed by advanced ATR correction; the abscissa of the graph was converted into wavelength to obtain the final graph. Using the min–max standardization method, the original spectral data were linearly transformed to the range of 0–1, and the calculation formula is

$$out = (in - \min(in)) / (\max(in) - \min(in))$$

where in and out are the input and output vectors, respectively, and $\min(x)$ and $\max(x)$ return the minimum and maximum values, respectively, of the input vector.

The similarity between the different spectra was evaluated by Pearson correlation coefficients (PCCs) and Euclidean distance.

The PCC is a statistical indicator that measures the correlation between two variables; it is defined as the quotient of the covariance and standard deviation with two variables. The PCC ranges in value from -1 to $+1$, where 0 indicates no correlation, negative values indicate negative correlations, and positive values indicate positive correlations. The greater the absolute value of the correlation coefficient, the stronger the correlation. The PCC is defined as follows:

$$\rho_{X,Y} = \frac{\text{cov}(X, Y)}{\sigma_X \sigma_Y} = \frac{E[(X - \mu_X)(Y - \mu_Y)]}{\sigma_X \sigma_Y}$$

Euclidean distance, also called the Euclidean metric, is a commonly used distance definition that refers to the true distance between two points in m-dimensional space. The Euclidean distance for two sets of vectors, $A(a_1, a_2, \cdots, a_n)$ and $B(b_1, b_2, \cdots, b_n)$.is defined as follows:

$$d(A, B) = \sqrt{(a_1 - b_1)^2 + (a_2 - b_2)^2 + \cdots + (a_n - b_n)^2}$$

The smaller the Euclidean distance between the vectors, the greater the similarity. The similarity between vectors A and B is defined as follows

$$E_{A,B} = \frac{1}{1 + d(A, B)}$$

Statistical Analysis: The results were reported as the means $\pm$ SD of three independent experiments using SPSS Statistics for Windows, version 17.0. *p*-values calculated by student's *t*-test and less than 0.05 were considered statistically significant. ***$p < 0.001$; **$p < 0.01$; *$p < 0.05$.

Supporting Information

Supporting Information is available from the Wiley Online Library or from the author.

Conflict of Interest

The authors declare no conflict of interest.

[1] a) J. A. Krall, F. Reinhardt, O. A. Mercury, D. R. Pattabiraman, M. W. Brooks, M. Dougan, A. W. Lambert, B. Bierie, H. L. Ploegh, S. K. Dougan, R. A. Weinberg, *Sci. Transl. Med.* **2018**, *10*, eaan3464; b) R. Sharma, P. Tobin, S. J. Clarke, *Lancet Oncol.* **2005**, *6*, 93.

[2] Y. K. Eddie, E. Mahnaz, *Application of Infrared to Biomedical Sciences*, Springer, Singapore **2017**.

[3] a) N. Hijnen, E. Kneepkens, M. de Smet, S. Langereis, E. Heijman, H. Grull, *Proc. Natl. Acad. Sci. U. S. A.* **2017**, *114*, E4802; b) Y. Lu, Q. Nan, J. Du, L. Li, A. Qiao, Y. Liu, *Int. J. Hyperthermia* **2010**, *26*, 316.

[4] a) Q. Chen, L. Xu, C. Liang, C. Wang, R. Peng, Z. Liu, *Nat. Commun.* **2016**, *7*, 13193; b) L. Guo, D. D. Yan, D. Yang, Y. Li, X. Wang, O. Zalewski, B. Yan, W. Lu, *ACS Nano* **2014**, *8*, 5670.

[5] U. Sassi, R. Parret, S. Nanot, M. Bruna, S. Borini, D. De Fazio, Z. Zhao, E. Lidorikis, F. H. Koppens, A. C. Ferrari, A. Colli, *Nat. Commun.* **2017**, *8*, 14311.

[6] F. Vatansever, M. R. Hamblin, *Photonics Lasers Med.* **2012**, *4*, 255.

[7] J. Ishibashi, K. Yamashita, T. Ishikawa, H. Hosokawa, K. Sumida, M. Nagayama, S. Kitamura, *Med. Oncol.* **2008**, *25*, 229.

[8] a) M. H. Falk, R. D. Issels, *Int. J. Hyperthermia* **2001**, *17*, 1; b) D. S. Kapp, G. M. Hahn, R. W. Carlson, *Principles of Hyperthermia*, 5th ed., B. C. Decker, Hamilton, Canada **2000**; c) J. van der Zee, *Lancet Oncol.* **2002**, *13*, 1173; d) P. Wust, B. Hildebrandt, G. Sreenivasa, B. Rau, J. Gellermann, H. Riess, R. Felix, P. M. Schlag, *Lancet Oncol.* **2002**, *3*, 487.

[9] a) K. Hasegawa, C. Negishi, F. Nakagawa, M. Ozaki, *J. Anesth.* **2012**, *26*, 168; b) B.-Y. Liau, T.-K. Leung, M.-C. Ou, C.-K. Ho, A. Yang, Y.-S. Lin, *Int. J. Photoenergy* **2012**, *2012*, 238468.

[10] K. Ogata, *System Dynamics*, 4th ed., Pearson, New York **2004**.

[11] H. Jang, Y. J. Park, X. Chen, T. Das, M. S. Kim, J. H. Ahn, *Adv. Mater.* **2016**, *28*, 4184.

[12] Y. Zhu, H. Ji, C. Cheng, R. S. Ruoff, *Natl. Sci. Rev.* **2018**, *5*, 90.

[13] Y. Hao, Y. Wang, L. Wang, Z. Ni, Z. Wang, R. Wang, C. K. Koo, Z. Shen, J. T. Thong, *Small* **2010**, *6*, 195.